Applied Physics Letters

Electromagnetic induction imaging with a scanning radio frequency atomic magnetometer

Cite as: Appl. Phys. Lett. **119**, 014001 (2021); https://doi.org/10.1063/5.0056876
Submitted: 15 May 2021 • Accepted: 18 June 2021 • Published Online: 06 July 2021

Cameron Deans, Yuval Cohen, Han Yao, et al.

Applied Physics Letters ARTICLE scitation.org/journal/apl

Electromagnetic induction imaging with a scanning radio frequency atomic magnetometer

Cite as: Appl. Phys. Lett. **119**, 014001 (2021); doi: 10.1063/5.0056876
Submitted: 15 May 2021 · Accepted: 18 June 2021 ·
Published Online: 6 July 2021

Cameron Deans,[a] Yuval Cohen, Han Yao, Benjamin Maddox, Antonio Vigilante, and Ferruccio Renzoni[b]

AFFILIATIONS

Department of Physics and Astronomy, University College London, Gower Street, London WC1E 6BT, United Kingdom

[a]**Present address:** RAL Space, STFC-Rutherford Appleton Laboratory, Fermi Avenue, Harwell, Didcot OX11 0QX, United Kingdom.
[b]**Author to whom correspondence should be addressed:** f.renzoni@ucl.ac.uk

ABSTRACT

We demonstrate electromagnetic induction imaging with an unshielded, portable radio frequency atomic magnetometer scanning over the target object. This configuration satisfies standard requirements in typical applications, from security screening to medical imaging. The ability to scan the magnetometer over the object relies on the miniaturization of the sensor head, the active compensation of the ambient magnetic field, and the implementation of a dedicated procedure to extract high-quality images from the recorded spatial dependent magnetic resonance. The procedure is shown to be effective in suppressing the detrimental effects of the spatial variation of the magnetic environment.

Electromagnetic induction imaging (EMI)[1] is a noncontact imaging technique, which allows for the spatial mapping of the electromagnetic properties of an object. Applications in security[2] and medical imaging[3–6] would greatly benefit from the inherently safe nature of the technique, due to the lack of ionizing radiation, while its technical simplicity makes it easily deployable, thus ideal for rapid assessment of brain injuries. EMI relies on the induction of eddy currents in the target by a low-frequency magnetic field and the measurements of the resulting secondary magnetic field. Conventional setups are based on pickup coils for the readout of the secondary field. However, this approach is limited by the poor sensitivity of coils at a low frequency, which has hindered the development of applications of EMI. The combination of EMI with ultra-sensitive atomic magnetometers (AMs)[7,8] has unlocked the potential of the technique, opening up a wealth of applications, from medical imaging,[9,10] to security and surveillance,[11–13] and industrial monitoring.

All experimental demonstrations to date[14–21] of electromagnetic induction imaging with atomic magnetometers (EMI-AM) rely on the displacement of the target object with respect to the fixed AM. Such arrangements are at odds with the requirements of imaging for many applications, where the ability to scan the sensor over the object is often needed. This is due to the technical difficulties associated with scanning AMs. First, recent realizations of EMI-AM rely on radio frequency atomic magnetometers (RF-AM),[22–25] which typically require two laser beams at different frequencies and a radio frequency source, hence are more difficult to miniaturize than, for example, coherent population trapping[27] or free-induction decay[28] magnetometers. An interesting route could be the adoption of technically simpler RF-AMs based on nonlinear magneto-optical rotation (NMOR),[26] although EMI with NMOR based RF-AMs has not been extensively explored.[8] Second, operation of an atomic magnetometer at extreme sensitivity requires a controlled environment. Typically, systems employ several layers of μ-metal shielding to suppress magnetic noise. This limits the scope of practical applications to targets within the shields. There have been many recent efforts to demonstrate the operation of AMs in unshielded environments.[29–34] Of direct interest to the present work, RF-AMs have been shown to retain their extreme sensitivity in unshielded environments.[35] This is usually achieved by compensating stray magnetic fields at the position of the AM. However, this results in an RF-AM that is optimized to a fixed position. Hence, until now, the EMI-AM procedure is simplified by keeping the AM fixed while moving the target.

In this Letter, we demonstrate EMI with an unshielded, portable RF-AM scanning over a fixed target object, thus satisfying the requirements for real-world applications. Our reported demonstration relies on two innovations. First, a compact RF-AM is realized with the sensor head including the required lasers sources, the RF source as well as the magnetic field coils for the active compensation of a stray magnetic field. Second, we note that the active compensation system used for stray magnetic fields cannot exactly cancel the magnetic environment.

Thus, a procedure is implemented to reduce the detrimental effects of the residual spatial variations in the magnetic environment experienced by the sensor head while scanning over the object.

Our sensor head follows the standard arrangement of an RF-AM, as sketched in Fig. 1. An atomic vapor is spin-polarized by optical pumping via a σ^+ laser beam in the presence of an applied bias magnetic field collinear to the laser beam. A perpendicular AC magnetic field ($\mathbf{B}_{RF}$) excites spin-coherences and produces a transverse atomic polarization. A linearly polarized probe laser beam is transmitted through the vapor, perpendicular to the pump beam. The atomic Larmor precession is mapped on the rotation of the probe plane of polarization, which is measured by a polarimeter. The output is then interrogated by a lock-in amplifier (LIA) and a spectrum analyzer.

The implementation of the sensor head is shown in Fig. 2. A support in nylon, 3D printed via selective laser sintering (SLS), holds all the optical and electronic parts in place, with a cover printed in the same material enclosing the sensor. A cubic glass cell of 25 mm side contains Rb vapor and 20 Torr of N_2, which acts as a buffer gas. Initial tests were carried out with a gently heated isotopically enriched ^{87}Rb vapor. However, a room temperature naturally occurring isotopic mixture of Rb was found to be sufficient for high-quality imaging and was installed and used for subsequent measurements. Two Vixar I0–0795S-0000-BC06 VCSEL lasers, with internal thermoelectric coolers (TECs) and thermistors, are integrated in the sensor head and provide pumping and probing light. Currents and temperatures are controlled by identical Thorlabs LDC200CV current supplies and Newport 325 temperature controller units.

The lasers are tuned by varying the current and temperatures but do not have independent control of frequency and intensity. The pump laser is tuned in resonance with the ^{87}Rb $5^2S_{1/2}, F = 1 \rightarrow 5^2P_{1/2}, F' = 2$ transition. For simplicity, and ease of retuning (normally required once a day), the probe is first tuned in resonance with the D_1 line $F = 1 \rightarrow F'$ manifold, and then the current is finely tuned by maximizing the amplitude of the atomic magnetic resonance used for sensing. These detunings are obtained with a current/temperature

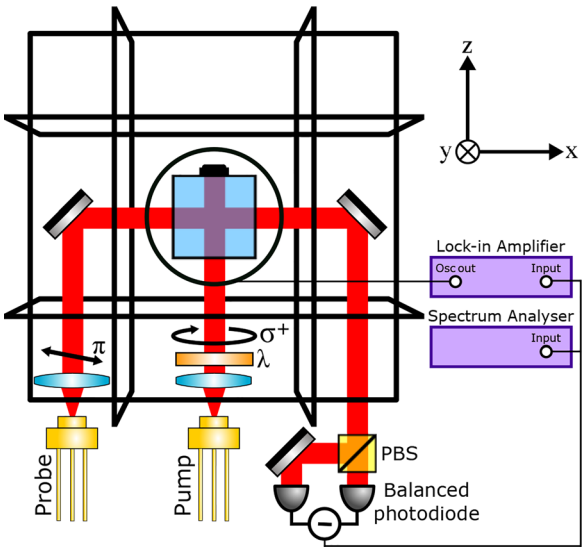

FIG. 1. Schematic overview of the magnetometer.

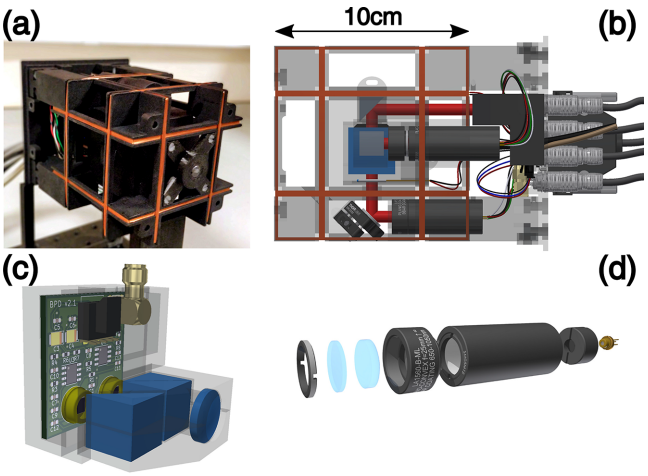

FIG. 2. (a) Photo of the sensor head, with the cover removed. (b) Computer-aided design (CAD) sketch of the magnetometer showing the two lasers, beam path, coils, cell, and electronic wiring. (c) The polarimeter. The probe enters after passing through the cell, where an F = 20 mm lens focuses the beam for detection. A polarizing beam splitter and a mirror direct the two separated components of polarization toward the two Thorlabs FDS100 photodiodes, separated by 14 mm and mounted on a PCB. The same PCB includes the differential amplification circuit. An SMA (SubMiniature version A) jack allows for readout of the output signal. The total volume of the polarimeter is 29.7 cm^3. (d) An exploded view of the Vixar I0-0795S-0000-BC06 VCSEL laser packaging. The chip output is collimated by an F = 25 mm lens. For the pump, a $\lambda/4$ waveplate is included to set the σ^+ polarization. The whole package is 18 mm in diameter and 45 mm in length.

settings, respectively, of 1.7 mA and 69.7° C for the probe and 2.0 mA and 70.4° C for the pump.

The sensor head also includes a system for the active compensation of spurious magnetic fields. A three-axis fluxgate magnetometer (Bartington MAG619) is placed near the cell and serves as an input for a feedback loop. Three proportional–integral–derivative (PID) modules (Standford Research Systems SIM960) drive current in three Helmholtz coil pairs (35 turns, 0.2 mm diameter copper wire, 10 cm side length) surrounding the sensor. The fluxgate magnetometer has a bandwidth of DC −3 kHz, limiting the bandwidth of the feedback loop, so ambient low-frequency magnetic noise is compensated for without affecting the applied radio frequency driving the magnetometer. The same system of coils used for the compensation of the ambient magnetic field is used to generate the bias magnetic field required for the operation of the RF-AM. This is implemented by introducing an appropriate voltage offset in the feedback loop acting on the Helmholtz coil pair in the bias field direction. The system is designed to produce a maximum magnetic field of 1.4×10^{-4} T at 250 mA along each orthogonal axis within the cell volume. This value is large enough to cancel any ambient magnetic fields and provide a bias field in the desired operating range—up to 100 kHz—regardless of the orientation of the sensor head.

The sensor head also includes a miniaturized balanced polarimeter. It contains a focusing lens (as in the figure description), a polarizing beam splitter (PBS), a mirror, and two photodiodes integrated on a printed circuit board (PCB) with the circuit for differential amplification. The total volume of the polarimeter is 29.7 cm^3. The dimensions and weight of the fully assembled head are 110 × 110 × 145 mm^3 and 1.49 kg, respectively.

The performance of the atomic magnetometer is evaluated by determining its sensitivity. For this, a 17 nT calibration field B_{RF} is applied. The RF field is scanned around resonance, and the polarimeter output is demodulated by a lock-in amplifier. The measured atomic magnetic resonance is displayed in Fig. 3(a), with the in-phase and out of phase lock-in amplifier outputs reported as a function of the detuning from resonance. The half-width at half-maximum (HWHM) of the atomic magnetic resonance is 460 Hz. Figure 3(b) shows the power spectrum of the polarimeter signal when the same field used in Fig. 3(a) is applied, with the reported baseline noise level obtained with the RF switched off. A signal to noise ratio (SNR) of 915 is extracted. From the presented data, we derive[35] an AC sensitivity $\delta B = B_{RF}/SNR$ of $19\,\mathrm{pT}/\sqrt{\mathrm{Hz}}$ and a DC sensitivity $\delta B = (\hbar/g\mu_B)(\Gamma/SNR)$, where $\hbar$ is Planck's constant, μ_B is the Bohr magneton, g is the Landé g-factor, and Γ is the full-width-at-half-maximum of the atomic magnetic resonance, of $22\,\mathrm{pT}/\sqrt{\mathrm{Hz}}$.

The active magnetic field compensation acts along the three directions, as any uncompensated ambient field would shift the magnetometer out of resonance. The most critical stabilization is along the bias field. We verified the effective operation of the feedback loop by applying a 30 Hz oscillating magnetic field and observing the PID correction signal. The appearance of an additional resonance, as shown in Fig. 3(c), shows that the PID reacts to the 30 Hz field and acts to cancel it.

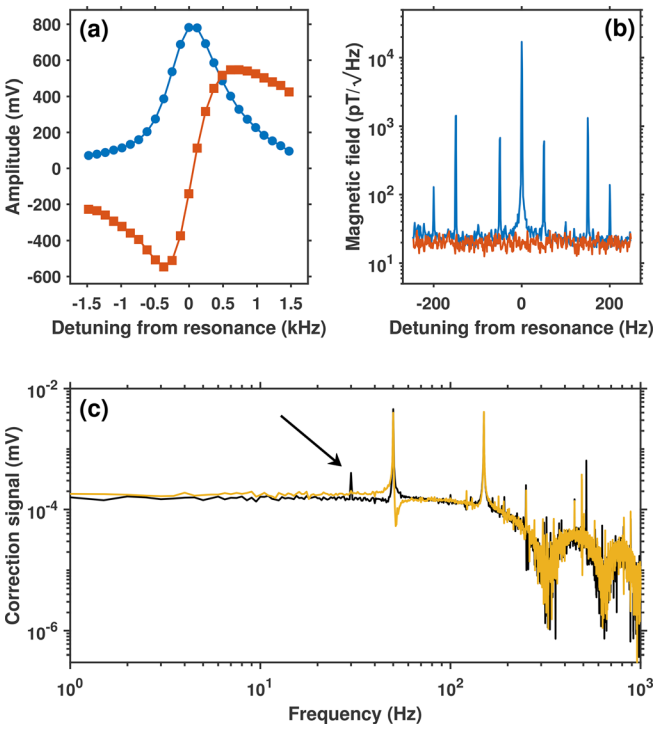

FIG. 3. (a) A typical atomic magnetic resonance from our system, in unshielded environment and with active stabilization, with the in-phase (blue circles) and out-of phase (red squares) signals obtained via demodulation of the polarimeter signal with a lock-in amplifier. The resonance shape was consistent over weeks, proving the high temporal stability of the instrument. (b) Power spectrum of a magnetometer signal, giving a signal to noise ratio of 915. (c) PID correction signal of the bias field stabilization in two different configurations: one operating in the ambient magnetic field (yellow) and the other (black) in the presence of an applied 30 Hz oscillating magnetic field, indicated by an arrow. Data are for a gently heated ($\simeq 40\,^{\circ}$C) isotopically enriched ^{87}Rb vapor and 20 Torr of N_2.

Imaging is performed by scanning the magnetometer over a target object held at a fixed position. The sensor head is mounted on a computer-controlled motorized XY stage. Target objects can be placed on a plastic sheet above the scanning magnetometer. Sensor-object distances in the range of 2–12 mm were considered with similar results. All the results reported here correspond to a sensor-object distance of 2 mm.

A first investigation was devoted to the study of the magnetic environment and specifically to its spatial dependence. An 11×11 pixel scan is taken in a $200 \times 200\,\mathrm{mm}^2$ plane without any target object. At each position, the RF was scanned, and the resonance frequency was determined. Two different sets of measurements were taken, the first one without active stabilization, which was then activated for the subsequent measurements. Results of this background mapping are presented in Fig. 4. Figure 4(a) illustrates the background with the feedback loop left open. A 25.6 kHz variation in resonance frequency is seen across the image. For this measurement, the output of the PID was manually adjusted to the value corresponding to the PID output at the center of the image with feedback closed. Figure 4(b) shows the effect of active compensation, as obtained by closing the three feedback loops: the variation in resonance frequency is reduced to 3.2 kHz. The residual inhomogeneity of the magnetic field is due to the unavoidable displacement between the fluxgate and sensing volume of the AM, which does not allow for a perfect compensation of the stray magnetic fields at the AM center. This is particularly affected by any field gradients. The detrimental effect of the spatial variation of the magnetic background is also highlighted in Figs. 4(c) and 4(d), where the

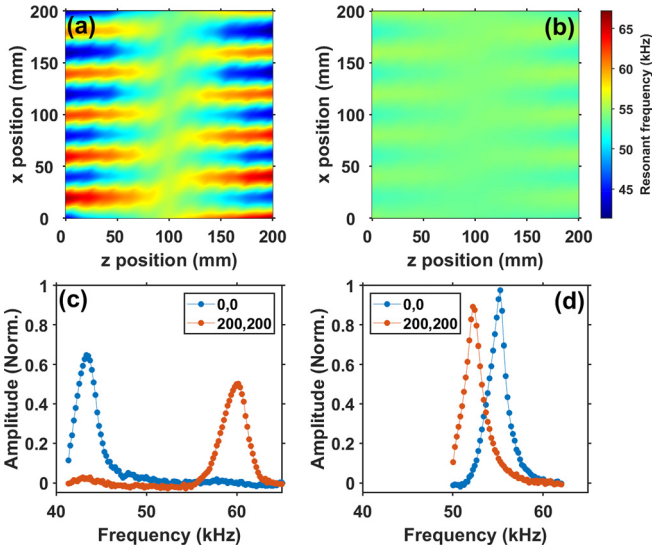

FIG. 4. Spatial map of the magnetic background. (a) and (b) Spatial dependence of the resonance frequency of the AM without (a) [with (b)] active compensation of the stray magnetic fields. (c) and (d) Atomic magnetic resonance at the two opposite edges of the imaged region, without (c) [with (d)] active compensation of the ambient magnetic field. The amplitude of the resonance is normalized to the maximum amplitude recorded in the image with active feedback. Data are for naturally occurring ^{85,87}Rb vapor and 20 Torr of N_2 at room temperature.

magnetic resonances at opposite edges (position 0,0 and 200,200 mm) of the images are measured without/with active compensation in operation. Active stabilization not only reduces the variation in the resonance frequency across the image but also increases the resonance amplitude.[35] A consistent background is thus crucial for imaging of conductive objects. While active compensation is essential, we will show in the following that additional procedures are required to obtain high-quality imaging with a scanning atomic magnetometer.

EMI was performed by scanning the magnetometer over the target sample. For each position, the rf frequency is scanned around resonance with the four outputs of the lock-in amplifier, the in-phase response (X), the quadrature response (Y), the amplitude of the response (R), and its phase lag (Φ), which are collected during the scan. The time required for a scan is dominated by the acquisition and processing time of the LIA, and by the time required by the XY stage to update the sensor position. For the presented data, a resonance sweep consists of 51 measurements with a 0.25 s acquisition time per point. An additional 0.9 s between resonance sweeps is taken by the XY stage to move the sensor to the new position. We note that a significant faster scanning can be obtained by only acquiring the polarimeter output traces and processing them on a computer. The active compensation of the magnetic field is not sufficient to reduce the level of the spatial variation of the magnetic environment. This is visible in Fig. 5(a), where an image of a copper square is produced by plotting the value of Y at the same frequency for all pixels. Lines across the image are due to the resonance frequency changing at different positions, as seen in the background scan shown in Fig. 4. High-quality imaging was obtained by adopting the following procedure, consisting of two elements. First, the resonance was tracked in the imaging: for each position, the magnetic resonance was fitted, and the total signal height (Y) at resonance was used, as opposed to at a set frequency. This significantly reduces the error in the determination of the resonance amplitude. The improvement in imaging performance is visible in Fig. 5(b). Second, the image is produced by introducing a detuning from resonance, and specifically taking the measurement for Y at +800 Hz detuning from resonance, a procedure initially established for low-conductivity imaging in the configuration with a fixed RF-AM.[16,18] This approach reduces the sensitivity to phase noise as measurements are taken in the wing of the atomic magnetic resonance, characterized by a reduced slope, and flattens the background further, producing a clear image of a copper square, as shown in Fig. 5(c).

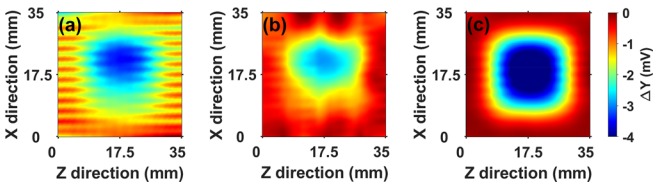

FIG. 5. Performance of resonance tracking and detuning for imaging. All images show Y and the colormaps are normalized to the scale on the right. All images are produced by using the same set of raw data generated by the lock-in amplifier. (a) The value of Y at 54 kHz is plotted. The resonant frequency for the image varies from a minimum of 53.8 to a maximum of 54.2 kHz, so the selected frequency corresponds to the central value. (b) Results obtained with resonance tracking. (c) Results obtained by introducing a detuning of +800 Hz from the tracked resonance. Data are for naturally occurring ^{85,87}Rb vapor and 20 Torr of N_2 at room temperature.

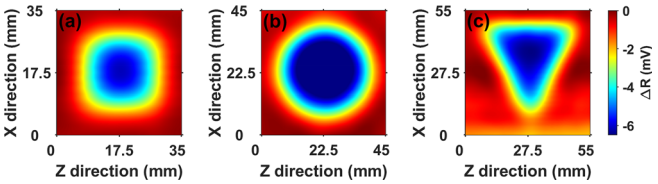

FIG. 6. Images of conductive objects. All image colormaps are normalized to the scale on the right. Parts (a) and (b) are taken with 1.5 mm step size, and part (c) is taken with 1.2 mm step size. Nearest-neighbor filtering helps with noise reduction in the image, with the data shown using a three nearest neighbor Gaussian filter. Data are for naturally occurring ^{85,87}Rb vapor and 20 Torr of N_2 at room temperature.

The imaging performance is illustrated in Fig. 6, which reports EMI images of a $25 \times 25 \times 1$ mm^3 Copper square, a 37 mm diameter 2 mm thick aluminum circle, and a 50 mm base and height, 2 mm thick aluminum isosceles triangle. All these images were taken with a scanning sensor head, active compensation of the magnetic field, and the procedure including the tracking of the resonance and near-resonant imaging. Data shown are for R, but similar images are also produced for X, Y, and Φ. All objects are clearly imaged, with their shapes well resolved. These images demonstrate the capability of performing EMI with a scanning radio frequency magnetometer. We note that none of the images presented in this work relies on background subtraction, further validating the use of the magnetometer in the field with no calibration.

In conclusion, in this work, we demonstrated electromagnetic induction imaging with a radio frequency atomic magnetometer scanning over target objects. The demonstration relies on a portable sensor head, with integrated laser sources, RF source and active compensation of ambient magnetic fields, and a dedicated imaging procedure that reduces the detrimental effects of the spatial variation of the magnetic environment.

The approach presented in this work is suitable for real-world applications, where the ability of scanning the sensor over the target object is typically a requirement. The technique does not require any background subtraction, thus further validating its applicability with to a variety of screening scenarios, from security to industrial monitoring and biomedicine.

We thank Roberto Cecchi (University of Siena) for sharing with us his circuit of the photodiode, which inspired our current design.

This work has been partially funded by the Future Aviation Security Solutions (FASS) programme, a joint Department for Transport and Home Office initiative, under Contract No. ACC6008813. With thanks for the technical oversight and programme management provided by the Defence Science and Technology Laboratory (Dstl). This research has also received funding from the UK Engineering and Physical Sciences Research Council (EPSRC) [Grant Nos. EP/P510270/1 (A.V.), EP/R512400/1 (Y.C.), and EP/N509590/1 (B.M.)].

DATA AVAILABILITY

The data that support the findings of this study are available from the corresponding author upon reasonable request.

REFERENCES

[1]H. Griffiths, "Magnetic induction tomography," Meas. Sci. Technol. **12**, 1126 (2001).
[2]B. J. Darrer, J. C. Watson, P. Bartlett, and F. Renzoni, "Magnetic imaging: A new tool for UK National Nuclear Security," Sci. Rep. **5**, 7944 (2015).
[3]S. Alzeibak and N. H. Saunders, "A feasibility study of in vivo electromagnetic imaging," Phys. Med. Biol. **38**, 151–160 (1993).
[4]R. Merwa, K. Hollaus, O. Biró, and H. Scharfetter, "Detection of brain oedema using magnetic induction tomography: A feasibility study of the likely sensitivity and detectability," Phys. Meas. **25**, 347–354 (2004).
[5]M. Zolgharni, H. Griffiths, and P. D. Ledger, "Frequency-difference MIT imaging of cerebral haemorrhage with a hemispherical coil array: Numerical modelling," Physiol. Meas. **31**, S111–S125 (2010).
[6]L. Wang and A. M. Al-Jumaily, "Imaging of lung structure using holographic electromagnetic induction," IEEE Access **5**, 20313–20318 (2017).
[7]A. Wickenbrock, F. Tricot, and F. Renzoni, "Magnetic induction measurements using an all-optical ^{87}Rb atomic magnetometer," Appl. Phys. Lett. **103**, 243503 (2013).
[8]A. Wickenbrock, S. Jurgilas, A. Dow, L. Marmugi, and F. Renzoni, "Magnetic induction tomography using an all-optical ^{87}Rb atomic magnetometer," Opt. Lett. **39**, 6367 (2014).
[9]L. Marmugi and F. Renzoni, "Optical magnetic induction tomography of the heart," Sci. Rep. **6**, 23962 (2016).
[10]C. Deans, L. Marmugi, S. Hussain, and F. Renzoni, "Optical atomic magnetometry for magnetic induction tomography of the heart," Proc. SPIE **9900**, 99000F (2016).
[11]L. Marmugi, S. Hussain, C. Deans, and F. Renzoni, "Magnetic induction imaging with optical atomic magnetometers: Towards applications to screening and surveillance," Proc. SPIE **9652**, 965209 (2015).
[12]C. Deans, L. Marmugi, and F. Renzoni, "Through-barrier electromagnetic imaging with an atomic magnetometer," Opt. Express **25**, 17911 (2017).
[13]C. Deans, L. Marmugi, and F. Renzoni, "Active underwater detection with an array of atomic magnetometers," Appl. Opt. **57**, 2346 (2018).
[14]C. Deans, L. Marmugi, S. Hussain, and F. Renzoni, "Electromagnetic induction imaging with a radio-frequency atomic magnetometer," Appl. Phys. Lett. **108**, 103503 (2016).
[15]A. Wickenbrock, N. Leefer, J. W. Blanchard, and D. Budker, "Eddy current imaging with an atomic radio-frequency magnetometer," Appl. Phys. Lett. **108**, 183507 (2016).
[16]L. Marmugi, C. Deans, and F. Renzoni, "Electromagnetic induction imaging with atomic magnetometers: Unlocking the low-conductivity regime," Appl. Phys. Lett. **115**, 083503 (2019).
[17]K. Jensen, M. Zugenmaier, J. Arnbak, H. Stærkind, M. V. Balabas, and E. S. Polzik, "Detection of low-conductivity objects using eddy current measurements with an optical magnetometer," Phys. Rev. Res. **1**, 033087 (2019).
[18]C. Deans, L. Marmugi, and F. Renzoni, "Sub-Sm^{-1} electromagnetic induction imaging with an unshielded atomic magnetometer," Appl. Phys. Lett. **116**, 133501 (2020).
[19]P. Bevington, R. Gartman, W. Chalupczak, C. Deans, L. Marmugi, and F. Renzoni, "Non-destructive structural imaging of steelwork with atomic magnetometers," Appl. Phys. Lett. **113**, 063503 (2018).
[20]P. Bevington, R. Gartman, and W. Chalupczak, "Imaging of material defects with a radio-frequency atomic magnetometer," Rev. Sci. Instrum. **90**, 013103 (2019).
[21]P. Bevington, R. Gartman, and W. Chalupczak, "Enhanced material defect imaging with a radio-frequency atomic magnetometer," J. Appl. Phys. **125**, 094503 (2019).
[22]D. Budker and M. Romalis, "Optical magnetometry," Nat. Phys. **3**, 227–234 (2007).
[23]I. M. Savukov, S. J. Seltzer, M. V. Romalis, and K. L. Sauer, "Tunable atomic magnetometer for detection of radio-frequency magnetic fields," Phys. Rev. Lett. **95**, 063004 (2005).
[24]W. Chalupczak, R. Godun, S. Pustelny, and W. Gawlik, "Room temperature femtotesla radio-frequency atomic magnetometer," Appl. Phys. Lett. **100**, 242401 (2012).
[25]W. Wasilewski, K. Jensen, H. Krauter, J. J. Renema, M. V. Balabas, and E. S. Polzik, "Quantum noise limited and entanglement-assisted magnetometry," Phys. Rev. Lett. **104**, 133601 (2010).
[26]M. P. Ledbetter, V. M. Acosta, S. M. Rochester, D. Budker, S. Pustelny, and V. V. Yashchuk, "Detection of radio frequency magnetic fields using nonlinear magneto-optical rotation," Phys. Rev. A **75**, 023405 (2007).
[27]P. D. D. Schwindt, S. Knappe, V. Shah, L. Hollberg, J. Kitching, L.-A. Liew, and J. Moreland, "Chip-scale atomic magnetometer," Appl. Phys. Lett. **85**, 6409 (2004).
[28]D. Hunter, S. Piccolomo, J. D. Pritchard, N. L. Brockie, T. E. Dyer, and E. Riis, "Free-induction-decay magnetometer based on a microfabricated Cs vapor cell," Phys. Rev. Appl. **10**, 014002 (2018).
[29]S. J. Seltzer and M. V. Romalis, "Unshielded three-axis vector operation of a spin-exchange-relaxation-free atomic magnetometer," Appl. Phys. Lett. **85**, 4804 (2004).
[30]R. J. Cooper, D. W. Prescott, P. Matz, K. L. Sauer, N. Dural, M. V. Romalis, E. L. Foley, T. W. Kornack, M. Monti, and J. Okamitsu, "Atomic magnetometer multisensor array for rf interference mitigation and unshielded detection of nuclear quadrupole resonance," Phys. Rev. Appl. **6**, 064014 (2016).
[31]G. Bevilacqua, V. Biancalana, Y. Dancheva, and L. Moi, "All-optical magnetometry for NMR detection in a micro-Tesla field and unshielded environment," J. Magn. Reson. **201**, 222 (2009).
[32]J. Belfi, G. Bevilacqua, V. Biancalana, S. Cartaleva, Y. Dancheva, and L. Moi, "Cesium coherent population trapping magnetometer for cardiosignal detection in an unshielded environment," J. Opt. Soc. Am. B **24**, 2357 (2007).
[33]D. A. Keder, D. W. Prescott, A. W. Conovaloff, and K. L. Sauer, "An unshielded radio-frequency atomic magnetometer with sub-femtoTesla sensitivity," AIP Adv. **4**, 127159 (2014).
[34]G. Bevilacqua, V. Biancalana, P. Chessa, and Y. Dancheva, "Multichannel optical atomic magnetometer operating in unshielded environment," Appl. Phys. B **122**, 103 (2016).
[35]C. Deans, L. Marmugi, and F. Renzoni, "Sub-picotesla widely-tunable atomic magnetometer operating at room-temperature in unshielded environments," Rev. Sci. Instrum. **89**, 083111 (2018).